Microspectroscopy on Thin Films of Colloidal Mixture Gradients for Data-Driven Optimization of Optical Properties

Marius Schöttle, Maximilian Theis, Tobias Lauster, Stephan Hauschild, and Markus Retsch*

Thin films comprising mixtures of different colloids provide a simple approach to materials with tunable optical properties. However, the prediction of UV–vis spectra for different compositions in colloidal crystals and glasses is difficult. The degree of disorder, for example, determines whether the optical response is dominated by incoherent scattering, coherent scattering, or Bragg diffraction. Both the volume ratio, as well as the morphology of the individual constituents, influence the properties of the ensemble, which necessitates extensive screening procedures. Here, a method for expediting such a screening approach by means of gradient colloidal crystals and glasses is shown. Continuous composition gradients, combined with local microspectroscopy, allow for the characterization of the entire composition range with high reproducibility, thereby reducing the experimental effort. This is shown for a system of spherical polymer particles with different radii. An optimum of the scattering efficiency in the visible wavelength range is shown close to the order/disorder transition at the edge of the composition range. The high-throughput screening method presented here can generate large data sets that may contribute to machine-learning-enabled optimization of self-assembled optical materials.

M. Schöttle, M. Theis, T. Lauster, M. Retsch
Department of Chemistry
Physical Chemistry I
University of Bayreuth
Universitätsstr. 30, 95447 Bayreuth, Germany
E-mail: markus.retsch@uni-bayreuth.de
S. Hauschild
Jülich Centre for Neutron Science (JCNS-1/IBI-8)
Forschungszentrum Jülich GmbH
52425 Jülich, Germany
M. Retsch
Bavarian Polymer Institute
Bayreuth Center for Colloids and Interfaces, and Bavarian Center for
Battery Technology (BayBatt)
University of Bayreuth
95447 Bayreuth, Germany

1. Introduction

The optical properties of non-absorbing, homogeneous bulk materials are intrinsic to the specific compound and provide little freedom for adjustment. Assemblies of colloidal microparticles, however, feature a high interface density and non-continuous refractive index (RI). This opens a variety of possibilities for engineered light-matter interactions. An especially interesting case is thin, particulate films, which lie in an intermediate regime between ballistic light transport and the opaque whiteness caused by multiple scattering.[1] These films play an important role in elementary applications such as paint or paper, as well as in coatings for electronics, solar cells, and radiative cooling.[2–4] The most common parameters governing the optical properties are the size, shape, and RI of the single particles, as well as the superordinate structure and filling fraction.[5,6] Inspiration can be found, for example, in the pronounced white appearance of highly scattering thin films in some beetle scales and butterfly wings.[1,7,8] Biomimetic approaches to efficient scattering have been presented in the form of porous structures built from silica or cellulose-based colloids.[9,10] Both shape anisotropy, as well as optimized Mie scattering are effective parameters, the latter providing the best results when the characteristic size is approximately half the wavelength of the incident light.[11] This morphological optimization allows the use of low-RI (< 1.7) materials that could replace potentially harmful titania nanoparticles.[12]

When using monodisperse, spherical colloids, various types of photonic materials can be fabricated. Ordered colloidal crystals, for example, exhibit a periodically changing refractive index. Ballistic light transport and interference cause angle-dependent structural colors.[13,14] However, if the strong immersion capillary forces and concomitant dense packing can be prevented during the assembly process, disordered colloidal glasses are obtained.[15] Structural coloration via dispersive light diffusion in such materials is attributed to Mie scattering of isomorphic particles and short-range order.[16–18] Colloidal glasses provide a versatile approach to tuning optical properties such as broadband reflectance or in anti-counterfeiting applications.[19–21] A

**ADVANCED
SCIENCE NEWS**

www.advancedsciencenews.com

**ADVANCED
OPTICAL
MATERIALS**

www.advopticalmat.de

simple route to these amorphous systems is the co-assembly of two particle sizes from a bi-disperse suspension.[22] While specific size ratios and compositions allow co-crystallization,[23] most combinations induce disorder. Binary particle monolayers have been prepared to determine optimum haze properties depending on the composition of large and small particles as well as the filling fraction.[24] These particle monolayers have also been utilized to specifically examine the transition from an ordered monodisperse system to the disordered binary case.[25] Spectroscopic analysis and simulations revealed the crossover from collective diffraction to single-particle scattering. 3D assemblies have also been characterized regarding their photonic, phononic, and thermal properties.[26,27] However, such screening approaches are tedious due to the large number of samples that must be prepared, especially if various combinations of different particle types are examined.

An efficient approach for screening the optical properties of colloidal materials has been shown for gold nanoparticles assembled in the form of a particle-size gradient.[28,29] Local spectroscopic characterization thereby allows large data sets to be obtained from a single sample. Continuous gradients in assemblies of microparticles are an emerging topic as well.[30–32] For example, structural analysis of the order to disorder transition has been shown via analytical ultracentrifugation.[33,34] However, an efficient platform tailored toward screening the optical properties of colloidal crystals and glasses has not been shown. We recently presented a method to gradient colloidal crystals via a modified vertical deposition method known as infusion-withdrawal coating (IWC).[35,36] Now, we present a screening platform based on leveraging the advantages of colloidal gradient compositions. Thin films formed from binary colloidal mixtures with a gradual composition gradient are examined via microspectroscopy. This provides a thorough analysis of the optical properties over the entire composition range. The large amount of UV–vis transmittance spectra provided by each gradient sample allows extensive data analysis. To directly correlate the optical transmittance with a specific composition, we introduce an orthogonal calibration technique based on two types of fluorescent tracer particles. Different combinations of relative particle diameters are shown to provide adjustable degrees of disorder and, thereby, tailored light scattering. We verify these results by additional measurements of colloidal assemblies with pre-defined layer thicknesses via patterned substrates. We find a markedly non-symmetric evolution of the scattering efficiency with the particle composition, indicative of an optimum scattering performance at the order-disorder transition of the large colloidal spheres. Furthermore, we expect this type of combinatorial sample preparation and characterization to expedite current research regarding the optical properties of particulate systems.
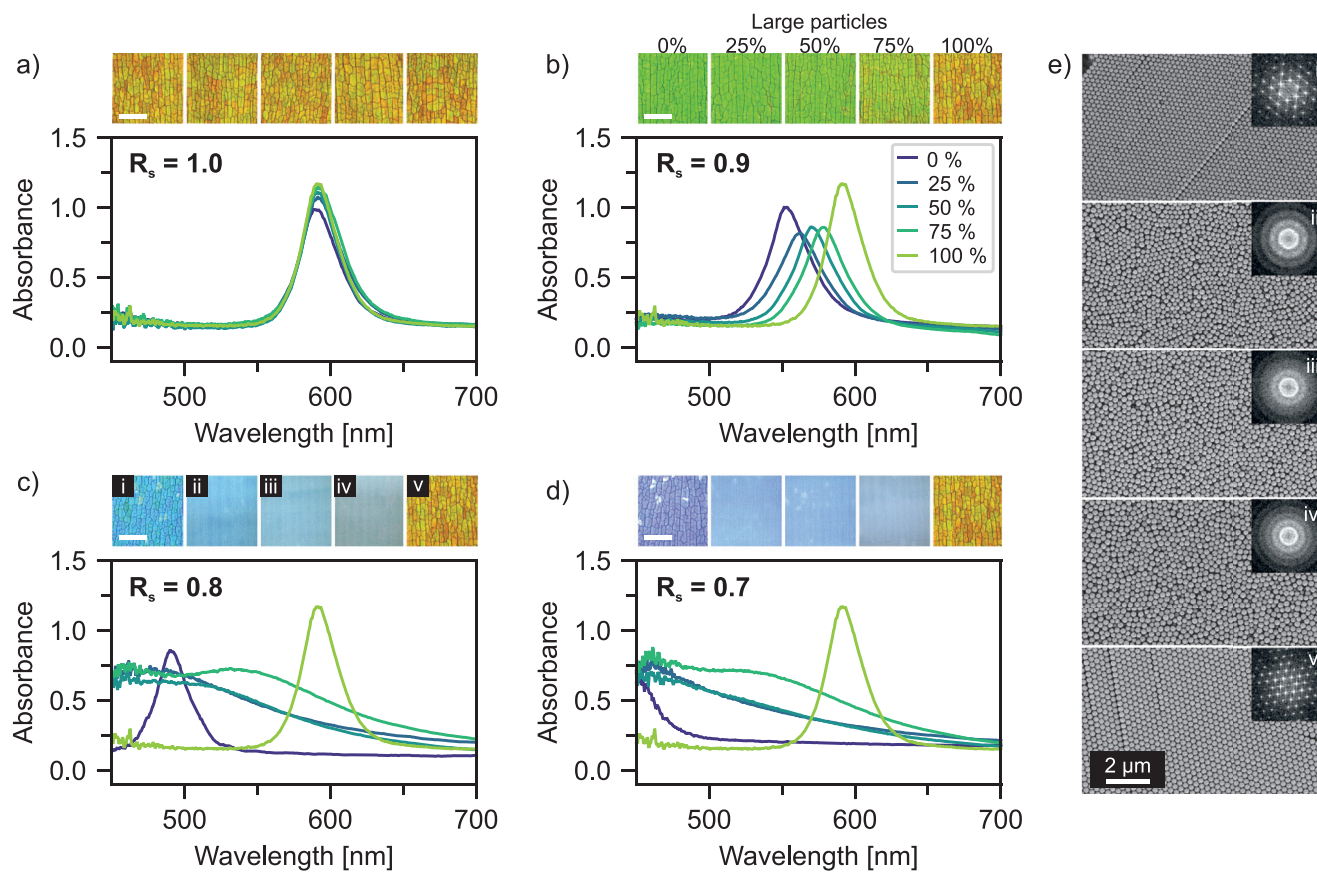
2. Results and Discussion

The system examined in this work is based on different combinations of poly(methyl methacrylate-co-n-butyl acrylate) (PMMA/nBA) particles. Four particle suspensions are prepared via surfactant-free emulsion polymerization with hydrodynamic diameters of 305, 282, 255, and 222 nm, respectively. Binary combinations of the largest particles with each of the three smaller

particles are fabricated via vertical deposition and characterized regarding the respective transmittance in the visible wavelength range. For the calibration of gradients, fluorescent tracers are prepared from the pristine particles via post-synthesis staining and added to the assemblies. Red fluorescent tracers are added to the large particles, and blue tracers to the smaller particles. Therefore, the ratio of red and blue fluorescence enables the accurate calibration of the composition. In **Figure 1**, we will discuss the optical properties of discrete (non-gradient) samples, and in **Figure 2**, the fluorescence-enabled calibration of gradient samples is presented. For the sake of clarity, we will use the term 'composition' for the binary particle mixture, which coincides with the ratio of red and blue fluorescent tracer particles.

For calibration reasons of the pursued methodology, we first fabricated discrete samples via vertical deposition of binary particle combinations on glass substrates (Figure 1). Each combination of particles is characterized by the according size ratio (R_s). As a proof of principle, samples consisting only of large particles ($R_s = 1.0$) with different compositions of blue and red tracers are also prepared (Figure 1a). The colloidal crystals formed from these monodisperse suspensions exhibit structural coloration and stop bands at approximately 600 nm. Importantly, the addition of fluorescent tracers does not affect the transmittance. The five spectra with different combinations of blue and red tracers are nearly identical. Mixing particles with similar diameters (Figure 1b, $R_s = 0.9$) also results in photonic colloidal crystals, but the optical properties change with the composition. The systems appear to accommodate the difference in particle size, retaining the periodic nature and allowing co-crystallization. The mean lattice spacing is reduced when adding smaller particles, and the color transitions from orange to green while the stop band shifts from 600 to 550 nm. A size ratio of 0.8 increases the level of disorder to the extent that binary systems cannot co-crystallize but rather form amorphous ensembles (Figure 1c). Reflectance microscopy images show vivid structural coloration only for the monodisperse samples but not for the mixtures. A difference can also be observed regarding the formation of micro-cracks. The density of cracks is much lower in the amorphous samples, and the crack orientation is mainly parallel to the coating direction. UV–vis absorbance spectra of the mixtures are dominated by diffuse scattering, which increases toward shorter wavelengths. An exception is the sample with 75% large particles, which shows a broad peak at 550 nm attributed to Mie scattering of the majority component. Similar observations can be made for $R_s = 0.7$ (Figure 1d). The binary mixtures are disordered, and the photonic glass peak of the 75% sample is slightly broader and less pronounced than for $R_s = 0.8$.

Scanning electron microscopy (SEM) of assemblies with $R_s = 0.8$ corroborate a periodicity of the monodisperse and an isotropic, disordered structure of the mixed case. Fast Fourier Transforms (FFT) of the images show a much more detailed structure factor when one particle type is the majority (25 and 75% large particles) as compared to the 50:50 mixture (Figure 1e; Figure S1, Supporting Information). This elucidates how dissimilar amorphous compositions can be and why a thorough optical characterization of the entire composition range is indispensable to fully understand the influence of disorder on the optical transmission properties. The discrete samples do not provide
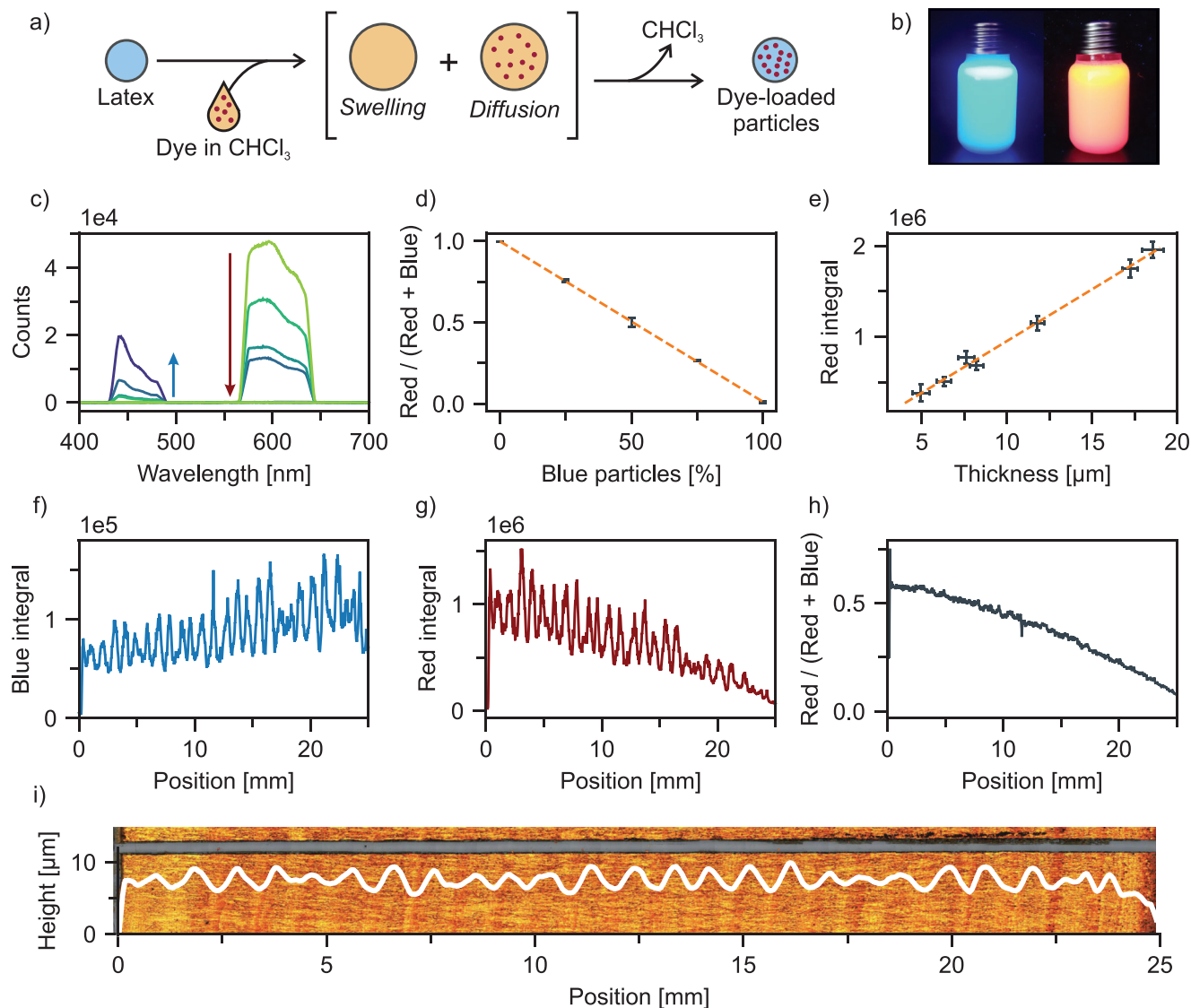
**ADVANCED
SCIENCE NEWS**

www.advancedsciencenews.com

**ADVANCED
OPTICAL
MATERIALS**

www.advopticalmat.de

Figure 1. Characterization of discrete samples of binary colloidal assemblies. a) UV–vis absorbance spectra and reflectance microscopy images of colloidal crystal thin films prepared from large particles with different compositions of added red and blue tracer particles. b–d) Analogous characterization of binary systems with several different size ratios (R_s). The composition here corresponds both to the relative amount of large and small particles as well as the relative amount of red and blue tracer particles. e) SEM images and corresponding Fast Fourier Transforms of the samples indicated in (c). The scale bar in microscopy images is 100µ m.

enough information for the entire picture, which necessitates the following use of gradient colloidal assembly as a suitable screening platform.

Fully continuous composition gradients ranging between a composition of zero to one can theoretically contain every possible binary combination of two particles. A broad screening of this range, as well as a detailed examination of a specific section, is possible and entails large data sets. Practically, these gradient samples are prepared via IWC, a dual syringe pump method that is a modified version of vertical deposition (Figure S2a, Supporting Information). The method used in this work does not produce linear gradients (Figure S2b, Supporting Information), which necessitates a post-fabrication correlation of the lateral position along the gradient and the corresponding composition. Fluorescence labeling presents an elegant, orthogonal calibration method that relies on an optical signal and is, therefore, non-invasive. Pristine PMMA/nBA particles are stained via a reversible swelling/diffusion mechanism (Figure 2a) with a solution of one of two different dyes (red and blue, Figure 2b; Figure S3, Supporting Information).[37] The resulting stained particles remain monodisperse, and self-assembly into colloidal crystals proceeds unhindered (Figure S4, Supporting Information). Since the size of the stained particles is identical to the pristine

ones, the tracers can be added at a total of 5 vol% without affecting the assembly process. The reference samples in Figure 1 are used to verify this approach. Independently acquired fluorescence spectra show how the blue signal increases and the red signal decreases as the composition changes (Figure 2c). The normalized ratio of the red and blue fluorescence signals is shown to correlate correctly with the applied composition (Figure 2d). The coincidence of the spectrally determined and gravimetrically controlled composition is a strong indication of the validity of the calibration technique. This holds for both crystalline assemblies (Figure S5a,b, Supporting Information) as well as disordered structures (Figure S5c,d, Supporting Information). An influence of the photonic properties on the fluorescence integral is not observed. Additionally, both the red and blue absolute fluorescence signals are shown to have a linear thickness dependency. This, in turn, ensures a thickness-independent determination of the composition (Figure 2e; Figure S6, Supporting Information).

To showcase the gradient calibration, we prepared a sample consisting only of large particles ($R_s = 1.0$) with a gradual change in the composition of red and blue tracer particles. Several thousand fluorescence microspectra are measured along the gradient, providing the red and blue fluorescence signal as a function of position (Figure 2f,g). Pronounced oscillations can be seen in

ADVANCED
SCIENCE NEWS
www.advancedsciencenews.com

ADVANCED
OPTICAL
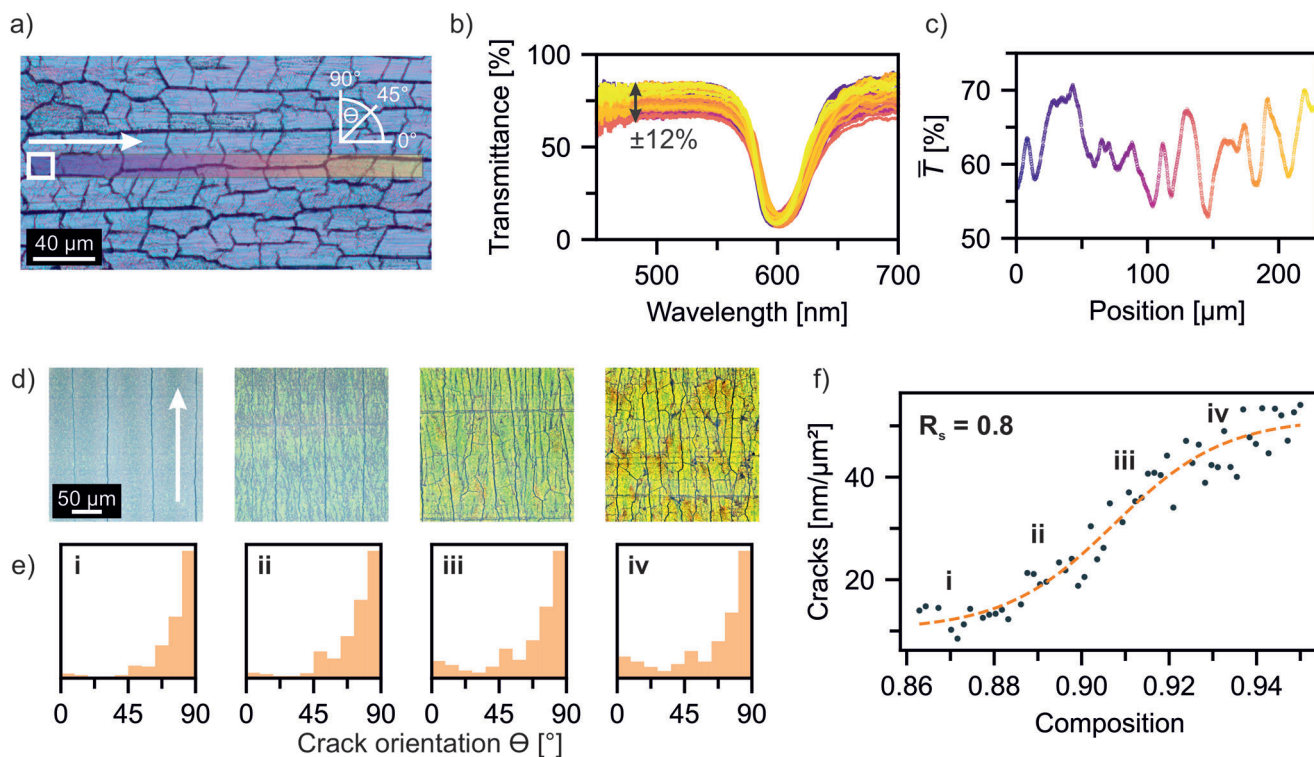**MATERIALS**
www.advopticalmat.de

Figure 2. Workflow elucidating how fluorescent tracer particles are used as a calibration of the particle composition. a) Schematic showing the post-synthesis staining. This provides tracer particles that can co-crystallize with the pristine particles and do not influence the colloidal crystal structure. b) Photograph of the stained particle suspensions under UV light. c) Fluorescence spectra of the samples in Figure 1a showing how the red fluorescence decreases and the blue fluorescence increases when the composition is changed. d) Corrected signal ratios showing a linear relation between fluorescence signal and particle composition. e) Linear dependence of the red fluorescence integral with respect to the sample thickness. f,g) Position-dependent fluorescence signals of a gradient colloidal crystal. h) Ratio of these fluorescence signals along the sample. This is used to correlate the position with the respective composition. i) Reflectance microscopy image of the gradient sample with an overlay showing the thickness profile along the coating direction. The thickness profile (white line) was measured via LSCM along the scratch shown at the top of the image, which was used as the reference for the height determination. Oscillations in the profile are caused by meniscus pinning during the assembly process.

both, which elucidates why the information from just one dye is not sufficient. The ratio of red and blue signals at each position (Figure 2h), however, provides a continuous signal with very little noise. A calibration curve can now be obtained that accurately maps the composition to the respective lateral position (Figure S7, Supporting Information). The oscillations in the pure red and blue curves can be explained by variations in the sample thickness (Figure 2i). The height profile obtained via laser scanning confocal microscopy (LSCM) along the gradient exhibits an oscillating thickness that occurs due to meniscus pinning during the coating process.[38] Fluorescence and thickness profiles

can be brought to a convincing overlap to verify this assumption (Figure S8, Supporting Information).

Besides the oscillations observed in the height profile, inhomogeneities on smaller length scales in the form of micro-cracks also play a role in colloidal systems. Transmittance microspectroscopy along a colloidal crystal shows the influence that these defects impose on the optical measurements (**Figure 3**a–c). While the stop band position and dip remain fairly constant, the baseline oscillates ± 12%. This is caused by wavelength-independent scattering at the edges of crystalline domains, which arise during the drying process.[39] For further analysis,

2300095 (4 of 11)

**ADVANCED
SCIENCE NEWS**

www.advancedsciencenews.com

**ADVANCED
OPTICAL
MATERIALS**

www.advopticalmat.de

Figure 3. Characterization of micro-cracks in colloidal crystals and glasses. a) Transmission microscopy image of a non-gradient colloidal crystal. The white square indicates the spot size of microspectroscopy (determined in Figure S9, Supporting Information), and the shaded area shows the measured path. b) Spectra measured along this path. c) Scatter plot of the average transmittance of these spectra in the visible range with respect to the position. d) Equidistant reflectance microscopy images of a gradient sample transitioning between a colloidal glass and crystal. The arrow indicates the coating direction, which corresponds to $\theta = 0°$. The gradient comprises a composition range of 0.85–0.95 with two particle types that have a size ratio of 0.8. The exemplary images shown here correspond to compositions of i) 0.86, ii) 0.90, iii) 0.93, and iv) 0.95, respectively. The difference in crack density and orientation of the cracks with respect to the coating direction are analyzed by image thresholding and a ridge detection algorithm. e) Distribution of the crack orientations in four evenly spaced regions along the sample. f) Crack density of all images correlated with the respective composition that was determined via the fluorescence-based calibration. The sigmoidal fit (orange) shows a gradual decrease of the crack density between compositions of 0.93 - 0.88 as the sample transitions from crystalline to amorphous.

the average transmittance over the visible range ($\overline{T}$) is plotted versus the position. This value fluctuates ± 10% with a frequency that fits well to the crack density. As it is obvious that the micro-cracks have a significant influence regarding the local optical characterization, we examined potential differences that occur regarding crack formation in colloidal crystals and glasses, respectively. Therefore, a gradient sample is prepared that specifically targets the transition region between order and disorder, which for $R_s = 0.8$ is found between 85% and 95% large particles. The gradient allows extensive analysis, and more than 60 positions are examined with reflectance microscopy (Figure 3d).

Each position can be mapped to the respective composition via calibration with the fluorescent tracer particles. Image analysis and crack characterization (Figure S10, Supporting Information) proceed with respect to both the crack density as well as the orientation of cracks. Equidistant positions show a gradual transition from the colloidal glasses with cracks exclusively parallel to the coating direction to more randomly distributed cracks in the crystalline case (Figure 3e). Simultaneously, the crack density increases by a factor of 5. It does so gradually, in a composition range between 0.88 and 0.93 (Figure 3f). Evaporation-induced assembly involves shrinkage upon drying. It thereby induces in-

plane stress, which, when the tensile strength is surpassed, dissipates via crack formation.[40,41] For most close-packed examples, these fractures occur along the 111 planes.[42] When transitioning to amorphous systems, however, no facets exist that facilitate crack propagation. Additionally, we expect a non-close packed system with a filling fraction <0.74 to enable local dissipation via reorganization. The fact that cracks parallel to the coating direction are most frequent in the crystalline case and dominate in the amorphous case is due to the most stress being developed parallel to the meniscus. This effectively tears the domains apart.[43] Besides enabling the analysis of the crack formation, the microscopy images of this gradient sample present a library of colors (Figure S11, Supporting Information) that are accessible simply by mixing the two particle types. In order to examine these optical properties in more detail, transmission UV–vis spectroscopy is performed along several gradient samples.

We start this gradient optical analysis with an assembly of monodisperse large particles ($R_s = 1.0$) with a gradient in the composition of added red and blue tracer particles. For example: a composition of 0.0 indicates 0% red particles and 100% blue particles. Several thousand transmittance spectra are obtained along this gradient and correlated both with the composition via
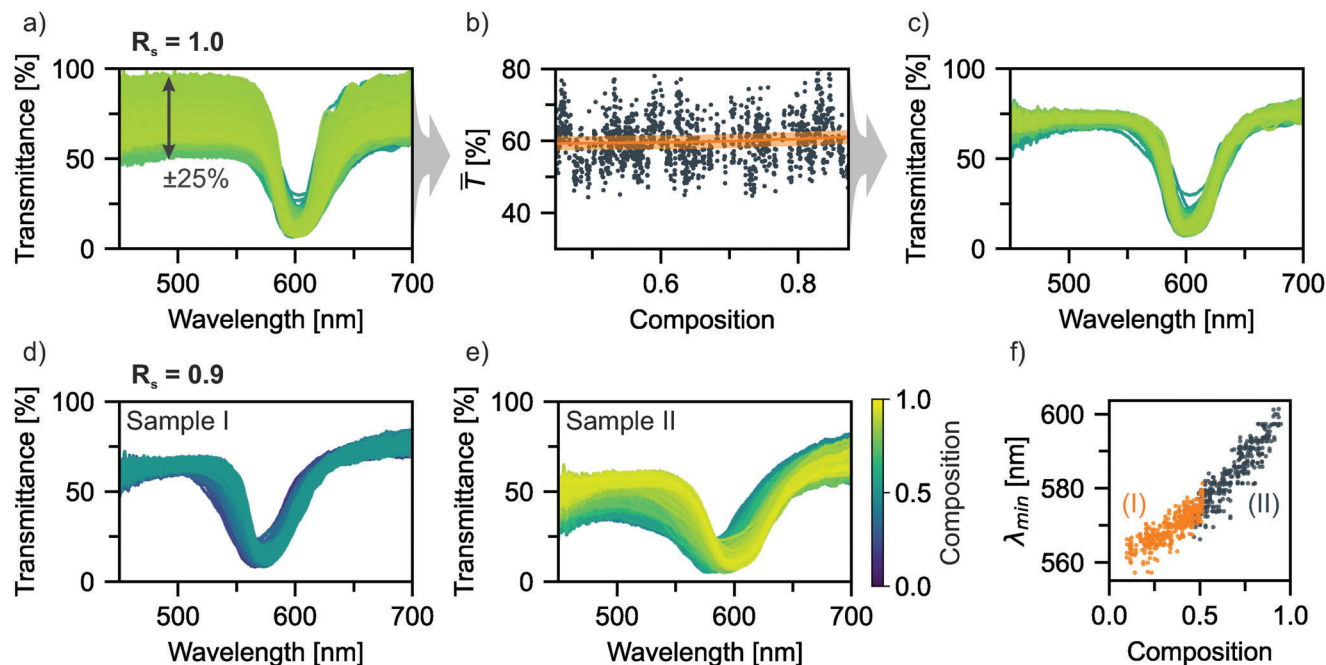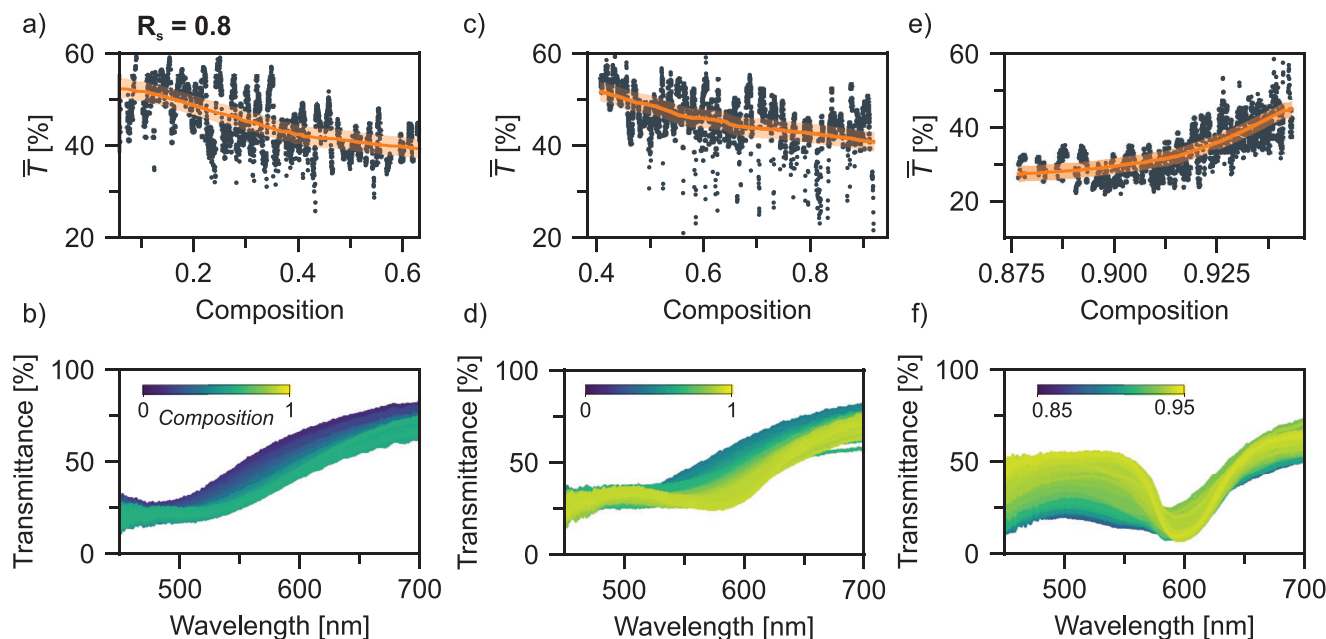
Figure 4. Microspectroscopic characterization of crystalline gradients. a) All transmittance spectra obtained along the coating direction of a sample consisting entirely of large particles with a gradient of the composition of red and blue tracer particles. The baseline shows strong oscillations due to scattering at micro-cracks and a modulated thickness. b) Average transmittance of all the spectra in (a), along with a first-order Savitzky–Golay filter in orange. By excluding all data that does not lie inside a 2% margin of the filter, only spectra from comparable positions along the sample remain. As shown in c), these consequently overlap very well. d,e) Filtered spectra obtained from two gradient samples consisting of two particles with a size ratio of 0.9 that show co-crystallization over the entire composition range. Only two samples are needed to cover the majority of this range and, as shown in f), allow a determination of the stop band position with respect to the composition.

fluorescence analysis as well as with the thickness obtained from LSCM. The spectra show strong fluctuations of the baseline (**Figure 4**a). Oscillations of the sample thickness, as well as the formation of micro-cracks, both have an impact on the local optical properties and result in this scattering of ±25%. The unwanted noise makes a comparison of adjacent measurement spots difficult. However, both the thickness oscillation as well as the crack formation occur at high but distinct spatial frequencies (see FFT in Figure S12, Supporting Information) compared to the gradual change in composition, which is stretched over the entire sample. A standard procedure to eliminate unwanted, high-frequency noise is the use of the Savitzky–Golay filtering algorithm.[44] The average transmittance is plotted as a function of the composition, which shows substantial noise (Figure 4b). The filter shown in orange is applied and remains at a constant value of approximately 60% over the entire composition range. Spectra that do not lie in a 2% margin of the filter profile are now excluded from further analysis. The remaining, filtered spectra overlap and do not exhibit these baseline fluctuations (Figure 4c). This elucidates how spectra are obtained with a similar influence of the micro-cracks and allows a more reasonable comparison of spectra along the sample. We applied this data filtering procedure to two gradient samples prepared from particles with R_s = 0.9, which together span almost the entire range of compositions (Figure 4d,e; Figures S13 and S14, Supporting Information). The filtered spectra show a gradual shift of the stop band toward shorter wavelengths as more of the small particles are present in the ensemble. Figure 4f shows the combined stop band position

with respect to the composition, which ranges between 560 and 595 nm. The data sets from the two samples converge and prove that co-crystallization of the two particles is indeed possible over the entire range. This information would require countless discrete samples but using the gradient colloidal assembly, only two experiments are necessary.

Next, gradient samples, transitioning from crystalline to amorphous regions, are examined. **Figure 5** shows the average transmittance, the filtering approach, and the filtered spectra for gradient colloidal assemblies with R_s = 0.8 (For raw data: see Figures S15–S17, Supporting Information). For most of the composition range, the average transmittance decreases monotonously with an increasing amount of large particles (Figure 5a–d). The origin of this trend becomes clear when observing the corresponding spectra. While diffuse scattering persists in all cases, the effect of Mie scattering of large particles becomes increasingly more visible as a shoulder that shifts toward longer wavelengths. A greater part of the visible spectrum is thereby affected by the material, and ballistic transport through the sample is minimized. This increase in the scattering efficiency progresses until a composition is reached where the system is capable of compensating for the defects and crystallizes. In Figure 5e,f, results are shown for a sample specifically prepared to target this order-to-disorder transition. Between compositions of 0.85 and 0.95, the stop band originating from the periodic crystalline structure evolves. Simultaneously, the baseline moves to substantially higher transmittance values. This is especially pronounced at shorter wavelengths, as the transition from

**ADVANCED
SCIENCE NEWS**

www.advancedsciencenews.com
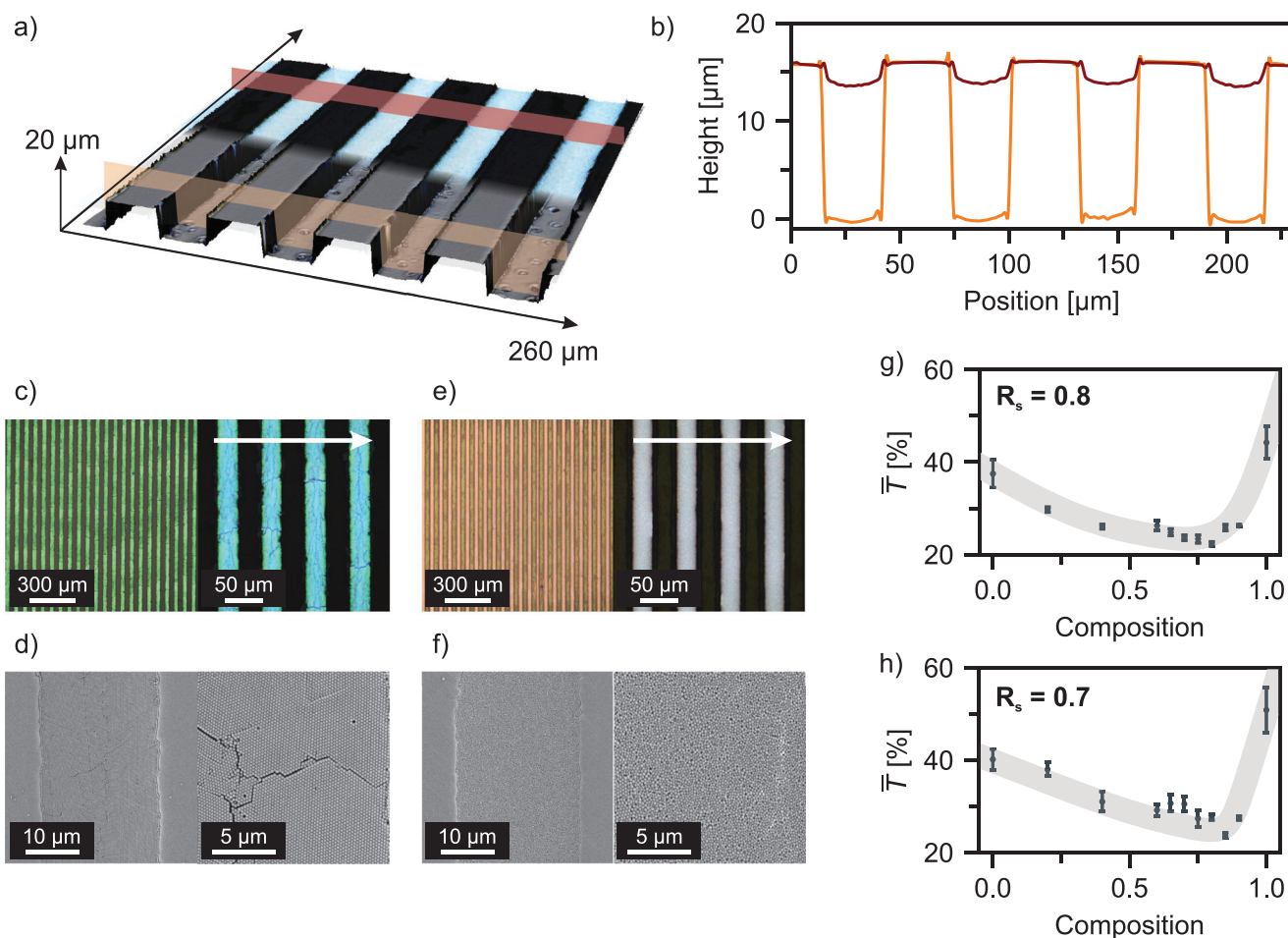
**ADVANCED
OPTICAL
MATERIALS**

www.advopticalmat.de

Figure 5. Microspectroscopic characterization of gradient samples ranging between crystalline and amorphous colloidal assemblies with a size ratio of $R_s = 0.8$. a) Average transmittance along the sample and b) filtered spectra. The shoulder in the spectra shifts to higher wavelengths as the amount of large particles increases, which explains the downward trend in (a). This trend persists when extending the composition range in (c) and (d). e,f) A sample designed to target the transition from order to disorder exhibits an increasing average transmittance as the composition approaches 1. The spectra show that this originates from less scattering at smaller wavelengths concomitant with the ballistic rather than diffusive light transport as the stop band begins to evolve.

diffusive to ballistic light transport reduces the number of scattered photons in this spectral range the most. The results show that an optimum of the scattering capability is found at a composition of approximately 0.9 for binary mixtures with $R_s = 0.8$. At this composition, a maximum of large particles are present, with enough small particles in the mixture to induce disorder. A correlation between the defect concentration caused by polydispersity and the reduction of the stop band intensity stands in accordance with results published for discrete samples.[45] The transition region observed via spectroscopy overlaps with the region observed in Figure 3f for the change of the micro-crack density. This stands to reason since both are attributed to an evolving crystallinity.

Gradient colloidal assemblies with a greater difference in particle size ($R_s = 0.7$) show a similar trend. An increasing amount of large particles results in more scattering over the entire visible spectrum and a monotonously decreasing average transmittance (Figures S18–S21, Supporting Information). However, even at a composition of 0.95, no stop band can be observed. The increased difference of the diameters compared to $R_s = 0.8$ causes greater disruption of the periodic structure, which cannot be accommodated as easily. Even minute addition of small particles hinders the crystallization of the large particles. Measuring beyond a composition of 0.95 is not possible on these samples due to macroscopic defects that compromise the structure at the beginning of the coating process. Additionally, another difference between crystalline and amorphous assembly can be found when observing the overall trend of the film thickness (Figure S22, Supporting Information). While purely crystalline or purely amorphous samples show a reasonably constant thickness (exclud-

ing the oscillations caused by meniscus pinning), this is not the case for the transition regime. Even though all external parameters, such as particle concentration, coating speed, and humidity, are constant, ordered assemblies from a monodisperse suspension result in considerably lower thicknesses compared to the bidisperse, amorphous case. Therefore, samples ranging between crystalline and amorphous show an overall trend in the film thickness. This must be taken into account, as the transmittance of light-scattering materials shows a pronounced thickness dependency.[5] We, therefore, confirm our findings based on the gradient assemblies with a selection of discrete samples that exhibit a defined film thickness.

The organization of colloids can be directed via topographically patterned substrates.[46] Self-assembly in 1D micro-trenches, for example, results in lines of colloidal crystals that exhibit a defined width and height, as dictated by the substrate and the shape of the meniscus.[47] Here we apply patterned, hydrophilized poly(dimethyl siloxane) (PDMS) substrates to ensure unimpeded optical transmittance. Colloidal crystals and glasses are selectively deposited in the trenches via vertical deposition from (mixed) suspensions (**Figure 6**a). Height profiles of both the empty trenches and the coated substrate (Figure 6b) indicate how the colloidal assembly proceeds in lines with 30 µm width and a height of 14 µm. Reflectance light microscopy and SEM images of monodisperse particles assembled in the trenches show structural coloration and the hexagonal structure of colloidal crystals (Figure 6c,d). This is the case for both small and large particles (Figure S24, Supporting Information). Analogous images are presented for an amorphous assembly (Figure 6e,f). Besides the more vivid structural coloration of the crystalline samples, it also

**ADVANCED
SCIENCE NEWS**

www.advancedsciencenews.com

**ADVANCED
OPTICAL
MATERIALS**

www.advopticalmat.de

Figure 6. Discrete colloidal assemblies in ridges of a topographically patterned substrate. a) 3D reconstructed images obtained via laser scanning confocal microscopy of an empty PDMS substrate (front) and a coated sample (back) (Separate data in Figure S23, Supporting Information). The orange and red cross sections indicate where the height profile shown in b) was evaluated. A height profile with x- and y-axis to scale is shown in Figure S26 (Supporting Information). c,d) Reflectance microscopy and scanning electron microscopy of the top surface of monodisperse particles assembled to colloidal crystals inside the micro-ridges. The arrow indicates the direction of the path along which UV–vis spectra are measured later. e,f) Analogous images for an amorphous mixture of large and small particles assembled on the substrate. g,h) Average transmittance obtained from discrete samples consisting of mixtures of particles with size ratios of 0.8 and 0.7. Each point is the mean value obtained from the UV–vis transmittance spectra measured in five consecutive ridges. Details regarding the measurement are shown in Figure S25 (Supporting Information). The grey lines are guides to the eye.

becomes obvious that amorphous assembly proceeds with little or no crack formation compared to the ordered case.

UV–vis transmission microspectroscopy of these samples is performed by slowly moving perpendicular to the trenches while acquiring spectra. In five consecutive trenches, a spectrum is chosen in the middle of each trench. This is possible by examining the position-dependent average transmittance which plateaus in this region (Figure S25, Supporting Information). This is done for several samples over the entire composition range for both $R_s = 0.8$ and 0.7. The average transmittance of all spectra is shown in Figure 6g,h. An analogous trend, as observed before for the continuous gradients, can be seen. With an increasing amount of large particles, the scattering efficiency increases, and the average transmittance shows a downward trend. At the point where self-assembly to crystalline structures is possible, ballistic transport dominates, and the average transmittance increases

strongly. The agreement between the large data sets procured from gradient colloidal assemblies with the measurements on thickness-controlled, patterned substrates shows how the two approaches are complementary. Comprehensive optical characterization of several particle size ratios and compositions was thereby possible, and the results were independently corroborated.

Since all measurements so far were conducted with a fairly high numerical aperture (and, therefore, also a high acceptance angle), we also examined this parameter. Scans along the gradient in Figure 5c,d ($R_s = 0.8$) were conducted with different objectives and acceptance angles between 29° and 67°. The mean transmittance of all three sets of microspectroscopy measurements shows identical trends (Figure S27, Supporting Information). A difference that can be seen, is that the measured transmittance is greater with a higher numerical aperture. This directly correlates with the higher acceptance angle, which,

**ADVANCED
SCIENCE NEWS**

www.advancedsciencenews.com

**ADVANCED
OPTICAL
MATERIALS**

www.advopticalmat.de

consequently, results in the detection of more scattered photons. Since the shape of the profile and the position of the minimum does not change when switching objectives, the assertions made in the previous sections hold true in this spectral range.

Finally, we performed a set of measurements to showcase the versatility of this approach and to touch on the possibilities opened by the optical screening platform. Machine learning-enabled prediction of structural color based on the specific geometry of dielectric arrays is becoming an important tool in the materials science community.[48] While in some cases, the training data can be obtained via simulations, other approaches require measured data. These data sets can become quite extensive, as was shown for the correlation of color and absorption spectra.[49] A set of images and spectroscopy data was used to train an artificial neural network and predict one from the other for a range of complex mixed oxides. This type of data structure can be obtained analogously with our gradient approach for the optical properties of binary colloidal mixtures. To increase the amount of information and allow a more complete characterization, both transmittance as well as reflectance microspectra and spectroscopy images were evaluated along a sample. A gradient with ($R_s = 0.8$), transitioning between order and disorder, was characterized this way (Figures S28– S31, Supporting Information). A qualitative evaluation of the data shows that both in reflection as well as transmission, the stop band begins to evolve between 88% and 92% large particles. For the reflectance measurements, this occurs earlier, which we attribute to a higher degree of order near the surface, masking a more disordered region underneath. While some pre-processing, such as filtering, is necessary, the output is a large number of correlated spectra and microscopy images. We expect that this approach will allow data-driven studies (i.e., machine learning) for tailored optical properties in complex systems of particle mixtures in the future.

3. Conclusion

We presented an integrated screening platform for the optical properties of binary colloidal mixtures. Thin films with a gradient of the particle composition were prepared. Fluorescent tracer particles were used as an orthogonal and non-invasive calibration routine to reveal the local particle composition with high lateral resolution. Mixing particles with a size ratio of $R_s = 0.9$ allowed co-crystallization over the entire composition range and showed a gradually shifting stop band. At $R_s = 0.8$, diffuse scattering dominated most parts of the particle composition, and light scattering proved to be most efficient when 90% large particles were present. A detailed examination of the transition regime between order and disorder was possible and elucidated the change from diffusive to ballistic light transport, which previously had been shown for a few discrete samples.[25,50] Further increase of the size difference at $R_s = 0.7$ induced disorder and pronounced light scattering even at minute addition of small particles. Finally, these results were verified by measuring transmittance spectra of discrete samples prepared with a defined thickness which was ensured via assembly on patterned substrates.

We expect this screening approach to go beyond the particle system presented here. Various mixtures are conceivable, such as organic/inorganic, spherical/anisotropic, or hollow/solid. This can be coupled with an evaluation of the respective structure fac-

tor via, reconstruction, scattering or simulations, and then allow theoretical studies of the optical properties.[51–54] Since measurements in the UV–vis, as well as the IR-range, can be performed locally, this will allow efficient screening of optimized colloidal materials for, for example, radiative cooling applications.[55–57] In a more general sense, obtaining large data sets is becoming increasingly important. Advanced analysis methods such as machine learning or Bayesian statistics are rapidly being improved and introduced into the field of materials science.[58] These rely on copious amounts of data which, in most cases, must be provided experimentally. Efficient screening techniques like the one presented in this work are, therefore, crucial to meet this requirement for implementing novel, data-driven analyses.

4. Experimental Section

Materials: Water used in this work was of Millipore quality. Methyl methacrylate (MMA 99%), n-butyl acrylate (nBA, 99%), sodium styrene sulfonate (NaSS, 99.99%), potassium persulfate (KPS, 99.99%), Nile red (NR), and Coumarin 1 (C1) were obtained from Sigma Aldrich. Chloroform was obtained from VWR. Poly(dimethyl siloxane) (PDMS) elastomer (SYLGARD 184) was obtained from Dow Corning.

Polymer Latex Synthesis: A 250 mL three-necked flask equipped with a reflux condenser and septa was loaded with 240 mL water and degassed for 75 min under a constant nitrogen stream at 80°C and 650 rpm stirring speed. With 5 min of homogenization time between each addition, the following reactants are added: 1) 7, 10, 13, or 16 mL of a 90:10 mixture of MMA/nBA, 2) 10 mg NaSS in 5 mL water, 3) 200 mg KPS in 5 mL water. The reaction was then allowed to proceed for 120 min before termination with ambient oxygen.

Particle Staining: Particle suspensions were diluted to 1.5wt% and 50 mL are stirred at 600 rpm. 5mg of either NR or C1 were dissolved in 1.5 mL chloroform and added dropwise. Stirring proceeds in a closed container for 24 h to allow swelling and diffusion of the dye. Subsequently, the lid was opened, and stirring was continued for 72 h to slowly remove the chloroform via diffusion and evaporation.[59] Finally, the suspensions were passed through a 5 μm syringe filter.

Assembly of Discrete Samples: Vertical deposition of discrete samples proceeded in a climate chamber set to 25°C and 75% relative humidity. Hellmanex III and plasma-cleaned glass substrates were dipped into particle suspensions of 1.0wt% that are stirred at 50 rpm. The substrate was then pulled out of the suspension at 0.25 μm s^{-1}.

Assembly of Gradient Samples: Gradient fabrication via infusion-withdrawal coating was done analogously to the discrete substrates except for the addition of two syringe pumps. The glass substrate was dipped into a suspension of one particle type with 1.0wt% and two cannulas attached to syringes were added to the system. One syringe pump extracts the suspension at 0.60 mL h^{-1}, the other infuses a suspension of a second particle type with 0.79wt% at 0.76 mL h^{-1}. The difference between the infusion and withdrawal speed was adjusted to account for the evaporation of water which was determined to be 0.16 mL h^{-1}. Thereby, both the water level as well as the particle concentration remain constant.

Assembly on Patterned Substrates: Masters for the patterned substrates were prepared via photo-lithography of SU8 resin on a silicon wafer by way of spin coating, soft bake, exposure at 365 nm (MaskAligner MJB4 by SUSS Microtec), post-exposure bake, development and hard bake. The two-component PDMS was cast on the wafer. Air bubbles were removed via vacuum treatment, and curing subsequently proceeded for 2h at 90°C. The PDMS substrates were then cut into 3×1cm pieces, hydrophilized in oxygen plasma for 5 s and immediately thereafter coated via vertical deposition, analogously to the flat substrates. The trenches were oriented parallel to the coating direction.

Microspectroscopy: Measurements proceed on an Olympus IX71 inverted microscope with a 40x Lens (N.A. 0.55). An OceanOptics USB4000 spectrometer was coupled via fiber optics. UV–vis spectra were obtained

**ADVANCED
SCIENCE NEWS**

www.advancedsciencenews.com

**ADVANCED
OPTICAL
MATERIALS**

www.advopticalmat.de

in transmission geometry with a halogen light source. The integration time was set to 100 ms. Fluorescence spectroscopy was performed on the same setup with a mercury vapor lamp in reflection geometry. For the red fluorescence, a Chroma 49004 ET Cy3 filter cube was used, allowing excitation between 530 and 560 nm and emission detection between 570 and 640 nm. The integration time was set to 10 ms, and 10 spectra were measured for averaging. For the blue fluorescence, a Chroma 49000 ET DAPI filter cube was used, allowing excitation between 325 and 375 nm and emission detection between 435 and 485 nm. The integration time was set to 100 ms. Gradient samples were moved at 100 μm s^{-1} with a motorized μm-stage while measuring. The sample was moved along the same path three times, to allow UV–vis and the two fluorescence measurements at analogous positions. UV–vis spectra along the patterned substrates are obtained analogously, but while moving at a speed of 5 μm s^{-1}.

Dynamic Light Scattering: Diluted dispersions were measured with a Zetasizer (Malvern) with 173° backscattering geometry.

Laser Scanning Confocal Microscopy: 2D color images and 3D reconstructions were obtained using a laser scanning microscope (Olympus, LEXT). High-magnification images were taken using a 50x lens (N.A. 0.95). Overview images were obtained by stitching images with a 5x lens (N.A. 0.15).

Scanning Electron Microscopy: Images were obtained with a Zeiss Leo 1530 (Carl Zeiss AG, Germany) at an operating voltage of 3 kV with in-lens detection after sputtering 2 nm platinum.

Data Analysis: The mean transmittance was determined from the UV–vis spectra by averaging the transmittance values between 450 and 700 nm. This was done for each spectrum and correlated with the respective position via the speed of the motorized stage and the time at which the spectrum was acquired. A correlation with the thickness at each position was thereby possible, and only spectra acquired in a specific range of thicknesses were examined (see Figures S13– S21, Supporting Information). A first-order Savitzky-Golay filter with a window length of approximately a third of the amount of spectra was applied, and for later characterization, only spectra that were in a range ± 2% of this filter were used for further characterization.

For both UV–vis as well as fluorescence spectroscopy, the integration time and number of spectra for averaging were adjusted so that the total time per acquired spectrum was always 100 ms, and measurement spots coincided. The blue fluorescence was integrated between 420 and 490 nm and the red fluorescence between 560 and 650 nm. Before each measurement, a sample comprising a 50:50 mixture of red and blue particles was measured as a reference. The ratio of the red and blue integral was used as a correction factor for the ratios determined from gradient samples.

Supporting Information

Supporting Information is available from the Wiley Online Library or from the author.

Conflict of Interest

The authors declare no conflict of interest.

Data Availability Statement

The data that support the findings of this study are available in the supplementary material of this article.

[1] G. Jacucci, L. Schertel, Y. Zhang, H. Yang, S. Vignolini, *Adv. Mater.* **2021**, *33*, 2001215.

[2] D.-Y. Zhou, X.-B. Shi, C.-H. Gao, S.-D. Cai, Y. Jin, L.-S. Liao, *Appl. Surf. Sci.* **2014**, *314*, 858.

[3] M. Karg, T. A. F. König, M. Retsch, C. Stelling, P. M. Reichstein, T. Honold, M. Thelakkat, A. Fery, *Mater. Today* **2015**, *18*, 185.

[4] J. Jaramillo-Fernandez, H. Yang, L. Schertel, G. L. Whitworth, P. D. Garcia, S. Vignolini, C. M. Sotomayor-Torres, *Adv. Sci.* **2022**, *9*, 2104758.

[5] S. Caixeiro, M. Peruzzo, O. D. Onelli, S. Vignolini, R. Sapienza, *ACS Appl. Mater. Interfaces* **2017**, *9*, 7885.

[6] G. Jacucci, J. Bertolotti, S. Vignolini, *Adv. Opt. Mater.* **2019**, *7*, 23.

[7] L. Cortese, L. Pattelli, F. Utel, S. Vignolini, M. Burresi, D. S. Wiersma, *Adv. Opt. Mater.* **2015**, *3*, 1337.

[8] B. D. Wilts, X. Sheng, M. Holler, A. Diaz, M. Guizar-Sicairos, J. Raabe, R. Hoppe, S. H. Liu, R. Langford, O. D. Onelli, D. Chen, S. Torquato, U. Steiner, C. G. Schroer, S. Vignolini, A. Sepe, *Adv. Mater.* **2018**, *30*, 1702057.

[9] M. S. Toivonen, O. D. Onelli, G. Jacucci, V. Lovikka, O. J. Rojas, O. Ikkala, S. Vignolini, *Adv. Mater.* **2018**, *30*, 1704050.

[10] G. Jacucci, B. W. Longbottom, C. C. Parkins, S. A. F. Bon, S. Vignolini, *J. Mater. Chem. C* **2021**, *9*, 2695.

[11] H. Yang, G. Jacucci, L. Schertel, S. Vignolini, *ACS Nano* **2022**, *16*, 7373.

[12] J. Hou, L. Wang, C. Wang, S. Zhang, H. Liu, S. Li, X. Wang, *J. Environ. Sci.* **2019**, *75*, 40.

[13] S. John, *Phys. Rev. Lett.* **1987**, *58*, 2486.

[14] J. D. Joannopoulos, P. R. Villeneuve, S. Fan, *Nature* **1997**, *386*, 143.

[15] P. D. García, R. Sapienza, C. López, *Adv. Mater.* **2010**, *22*, 12.

[16] J. F. Galisteo-López, M. Ibisate, R. Sapienza, L. S. Froufe-Pérez, A. Blanco, C. López, *Adv. Mater.* **2011**, *23*, 30.

[17] S. F. Liew, J. Forster, H. Noh, C. F. Schreck, V. Saranathan, X. Lu, L. Yang, R. O. Prum, C. S. O'Hern, E. R. Dufresne, H. Cao, *Opt. Express* **2011**, *19*, 8208.

[18] E. S. A. Goerlitzer, R. N. Klupp Taylor, N. Vogel, *Adv. Mater.* **2018**, *30*, 1706654.

[19] P. N. Dyachenko, J. J. do Rosário, E. W. Leib, A. Y. Petrov, R. Kubrin, G. A. Schneider, H. Weller, T. Vossmeyer, M. Eich, *ACS Photonics* **2014**, *1*, 1127.

[20] G. Shang, Y. Häntsch, K. P. Furlan, R. Janßen, G. A. Schneider, A. Petrov, M. Eich, *APL Photonics* **2019**, *4*, 4.

[21] L. Bai, Y. Lim, Y. He, Q. Xiong, S. Hou, J. Zhang, H. Duan, *Adv. Opt. Mater.* **2020**, *8*, 24.

[22] P. D. García, R. Sapienza, A. Blanco, C. López, *Adv. Mater.* **2007**, *19*, 2597.

[23] N. Vogel, L. de Viguerie, U. Jonas, C. K. Weiss, K. Landfester, *Adv. Funct. Mater.* **2011**, *21*, 3064.

[24] J. Semmler, K. Bley, R. N. Klupp Taylor, M. Stingl, N. Vogel, *Adv. Funct. Mater.* **2019**, *29*, 4.

[25] S. G. Romanov, S. Orlov, D. Ploss, C. K. Weiss, N. Vogel, U. Peschel, *Sci. Rep.* **2016**, *6*, 27264.

[26] T. Still, W. Cheng, M. Retsch, R. Sainidou, J. Wang, U. Jonas, N. Stefanou, G. Fytas, *Phys. Rev. Lett.* **2008**, *100*, 194301.

[27] F. A. Nutz, A. Philipp, B. A. F. Kopera, M. Dulle, M. Retsch, *Adv. Mater.* **2018**, *30*, 1704910.

[28] M. B. Müller, C. Kuttner, T. A. Konig, V. V. Tsukruk, S. Forster, M. Karg, A. Fery, *ACS Nano* **2014**, *8*, 9410.

[29] C. Kuttner, V. Piotto, L. M. Liz-Marzán, *Chem. Mater.* **2021**, *33*, 8904.

[30] S. H. Kim, W. C. Jeong, H. Hwang, S. M. Yang, *Angew. Chem., Int. Ed.* **2011**, *50*, 11649.

[31] H. Ding, C. Liu, H. Gu, Y. Zhao, B. Wang, Z. Gu, *ACS Photonics* **2014**, *1*, 121.

[32] M. Schöttle, T. Lauster, L. J. Roemling, N. Vogel, M. Retsch, *Adv. Mater.* **2022**, 2208745.

[33] M. Chen, H. Cölfen, S. Polarz, *ACS Nano* **2015**, *9*, 6944.

[34] M. Chen, K. Hagedorn, H. Cölfen, S. Polarz, *Adv. Mater.* **2017**, *29*, 1603356.

[35] M. Schöttle, T. Tran, T. Feller, M. Retsch, *Adv. Mater.* **2021**, *33*, 2101948.

[36] F. Ye, C. Cui, A. Kirkeminde, D. Dong, M. M. Collinson, D. A. Higgins, *Chem. Mater.* **2010**, *22*, 2970.

[37] J. H. Lee, I. J. Gomez, V. B. Sitterle, J. C. Meredith, *J. Colloid Interface Sci.* **2011**, *363*, 137.

[38] G. Lozano, H. Miguez, *Langmuir* **2007**, *23*, 9933.

[39] B. Hatton, L. Mishchenko, S. Davis, K. H. Sandhage, J. Aizenberg, *Proc. Natl. Acad. Sci. USA* **2010**, *107*, 10354.

[40] W. B. Russel, *AIChE J.* **2011**, *57*, 1378.

[41] W. P. Lee, A. F. Routh, *Langmuir* **2004**, *20*, 9885.

[42] K. R. Phillips, C. T. Zhang, T. Yang, T. Kay, C. Gao, S. Brandt, L. Liu, H. Yang, Y. Li, J. Aizenberg, L. Li, *Adv. Funct. Mater.* **2019**, *30*, 26.

[43] Y. Xu, G. K. German, A. F. Mertz, E. R. Dufresne, *Soft Matter* **2013**, *9*, 14.

[44] S. R. Krishnan, C. S. Seelamantula, *IEEE Trans. Signal Process.* **2013**, *61*, 380.

[45] R. Rengarajan, D. Mittleman, C. Rich, V. Colvin, *Phys. Rev. E: Stat., Nonlinear, Soft Matter Phys.* **2005**, *71*, 016615.

[46] N. Vogel, M. Retsch, C.-A. Fustin, A. del Campo, U. Jonas, *Chem. Rev.* **2015**, *115*, 6265.

[47] J. Li, S. Luan, W. Huang, Y. Han, *Colloids Surf., A* **2007**, *295*, 107.

[48] Z. Huang, X. Liu, J. Zang, *Nanoscale* **2019**, *11*, 21748.

[49] H. S. Stein, D. Guevarra, P. F. Newhouse, E. Soedarmadji, J. M. Gregoire, *Chem. Sci.* **2019**, *10*, 47.

[50] D. S. Wiersma, *Nat. Photonics* **2013**, *7*, 188.

[51] L. Schertel, L. Siedentop, J. Meijer, P. Keim, C. M. Aegerter, G. J. Aubry, G. Maret, *Adv. Opt. Mater.* **2019**, *7*, 15.

[52] G. Shang, K. P. Furlan, R. Janssen, A. Petrov, M. Eich, *Opt. Express* **2020**, *28*, 7759.

[53] V. Hwang, A. B. Stephenson, S. Barkley, S. Brandt, M. Xiao, J. Aizenberg, V. N. Manoharan, *Proc. Natl. Acad. Sci. USA* **2021**, *118*, 4.

[54] K. Shavit, A. Wagner, L. Schertel, V. Farstey, D. Akkaynak, G. Zhang, A. Upcher, A. Sagi, V. J. Yallapragada, J. Haataja, B. A. Palmer, *Science* **2023**, *379*, 695.

[55] J. Jaramillo-Fernandez, G. L. Whitworth, J. A. Pariente, A. Blanco, P. D. Garcia, C. Lopez, C. M. Sotomayor-Torres, *Small* **2019**, *15*, 1905290.

[56] H. H. Kim, E. Im, S. Lee, *Langmuir* **2020**, *36*, 6589.

[57] Y. Fu, Y. An, Y. Xu, J.-G. Dai, D. Lei, *EcoMat* **2022**, *4*, 12169.

[58] A. Ludwig, *npj Comput. Mater.* **2019**, *5*, 1.

[59] A. Steinhaus, R. Chakroun, M. Mullner, T. L. Nghiem, M. Hildebrandt, A. H. Gröschel, *ACS Nano* **2019**, *13*, 6269.